# Fatigue and fracture of small cracks in superelastic Nitinol

Louis G. Malito [a,*], Behrouz Haghgouyan [a], Matthew L. Bowers [a], Alfred Rosen [a], Behnam Amin-Ahmadi [b], Scott W. Robertson [c], Robert O. Ritchie [d]

[a] Exponent Inc, Menlo Park, CA 94025, USA
[b] Confluent Medical Technologies, Fremont, CA 94539, USA
[c] Resonetics, Nashua, NH 03060, USA
[d] Department of Materials Science & Engineering, University of California, Berkeley, CA 94720, USA

A B S T R A C T

The present study develops a hybrid total life and damage-tolerant fatigue methodology for the determination of a small crack growth threshold in Nitinol. Axial tension–tension/Mode I fatigue testing was performed on superelastic Nitinol wire specimens with starter cracks milled into the specimens using focused ion beam (FIB). Fatigue testing was performed in displacement control at various strain amplitudes, typical for Nitinol fatigue characterization given its superelastic behavior. The simplistic geometry of the test specimen and axial loading conditions also allowed for the calculation of stress amplitude and initial stress intensity factor range. A logistic regression analysis was used to determine strain/stress-based fatigue limits. The small crack growth threshold for superelastic Nitinol was obtained for the first time from physically small cracks with sizes comparable to native inclusions. Lastly, a fractographic analysis was performed to examine crack initiation and propagation from the FIB-milled starter cracks and to identify relevant fractographic features. While the proposed methodology is centered around the use case of Nitinol medical devices, it could be adapted for other materials and applications where small crack initiation and propagation play an important role in fatigue lifetime prediction.

## 1. Introduction

NiTi or Nitinol is a near-equiatomic alloy of nickel and titanium that remains a metallic material of choice for use in endovascular and cardiovascular implantable medical device applications. These applications and devices include guide wires, inferior vena cava filters, peripheral stents, heart valve replacement frames, and many others [1]. In such applications, Nitinol is used for its superelastic properties, that is the ability to recover large deformations or strains. The superelastic nature of Nitinol is exploited when an implantable device is inserted into the body in a low-profile, minimally invasive delivery system and then deployed through self-expansion at the repair or injury site. Once implanted, these devices are subjected to mechanical fatigue cycling from various anatomical boundary conditions, such as pulsatile loading from the cardiac rhythm cycle [2]. Implantable Nitinol devices must then be able to withstand hundreds of millions of fatigue cycles during their service life. A deep understanding of the mechanical and structural fatigue behavior of Nitinol is therefore critical to ensuring successful device development.

Numerous studies have been published investigating the fatigue properties of biomedical superelastic Nitinol [3–20]. These studies typically employ the total life methodology for fatigue. Fracture mechanics-based approaches such as damage tolerance have been used, although the size scale of test coupons and pre-cracking used is much greater than those typical of the structural elements in a stent [14,21–24]. In total life fatigue testing of Nitinol, an *S-N*, or strain amplitude *vs.* cycles to failure, curve is generated for a fixed mean strain and initial pre-strain conditions. Pre-straining before fatigue testing is done to simulate device insertion and deployment from a delivery system. This sequence of loading and unloading history is important to consider for a material like Nitinol to accurately represent the stress state. Strain is measured instead of stress due to the non-linear nature of the martensitic phase transformation in Nitinol. In the total life approach, the cycles to failure are inclusive of the cycles to initiate a crack and the cycles to propagate the crack to fracture.

Non-metallic inclusions (NMIs) often act as initiation sites for fatigue cracks in superelastic Nitinol. These inclusions are natural byproducts of the physical melting process and are further broken up and distributed

by forging and drawing operations [25]. Consequently, there has been much interest in understanding how the size and distribution of NMIs correlate to the mechanical fatigue properties of Nitinol. Several studies have demonstrated that the general reduction in the size and distribution of NMIs can increase fatigue life in Nitinol [4,7,10,26]. Different methods for the reduction in NMIs have been implemented, including starting ingot material purity, size, and processing methods [4].

Reducing the size and distribution of NMIs is one method of trying to solve the fundamental issue in the fatigue behavior of Nitinol medical devices – the small-crack initiation and growth phenomenon. Small cracks in this context refer to cracks that are comparable to the size scale of the inclusions in the material [27,28]. Literature studies have generally taken one of three approaches to understand small crack behavior in Nitinol. Studies have extrapolated small-crack growth thresholds from large-crack damage-tolerant fatigue data [22], have postulated small-crack thresholds from the size of NMIs that caused fatigue fracture in total life fatigue tests [16], or have estimated crack growth thresholds from hardness data [18]. Each method has its advantages and disadvantages in terms of both experimental implementation and the produced results.

Total life fatigue is advantageous for its simplicity in terms of testing and outcome. Specimens are designed to mimic, or are harvested from, actual devices and therefore maintain device geometry and processing conditions. Specimens are simply monitored for fracture during the test. As a result, it is impossible to monitor or discern crack initiation and crack growth cycles. Discontinuities that initiate fatigue fracture can only be analyzed post-mortem. Damage-tolerant fatigue testing enables physical monitoring of length and crack growth during testing; however, traditional specimen geometries exceed the size scales representative of implantable medical devices. Therefore, any crack growth thresholds measured from this method would be for large-crack growth. Small-crack growth thresholds are typically below those of large-crack thresholds in metallic materials [22,28]. This motivates the development of a method that combines the benefits of total life fatigue (*i.e.*, specimen geometry and simple implementation) with the direct crack measurement enabled by the damage-tolerant fatigue approach to study small-crack behavior in superelastic Nitinol.

This study aims to evaluate the small crack growth threshold in superelastic Nitinol. We evaluate the small crack growth threshold through a hybrid total life and damage-tolerant fatigue testing approach. Flaws of known dimensions were created in high-purity Nitinol wire through focused ion beam (FIB) milling to simulate starter fatigue cracks. These starter cracks are larger than native inclusions but are less than 0.1 % of the total cross-sectional area of the wire. The FIB-milled Nitinol wires were then axial tension–tension fatigue tested to determine the strain/stress amplitudes and mean strain/stress that correspond to a Mode I loading fatigue fracture. The combined knowledge of the initial crack size from FIB milling and the cyclic stress/strain history allows for the extrapolation of an initial stress intensity factor range. The initial stress intensity factor ranges that yielded runouts were analyzed to determine a small crack growth threshold. A fractographic analysis was performed to confirm the original size of the FIB-milled starter crack and to examine relevant fractographic features.

## 2. Background

Assessing resistance of a material to cyclic loading is achieved by monitoring the "total life" of specimens under various applied stresses (stress-life or *S-N* approach) or strains (strain-life or *ε-N* approach) [29]. Distinguishing between the life spent in initiation of a crack versus its growth can be important when material discontinuities are present. The "damage-tolerant" approach was developed to address this uncertainty and relies on fracture mechanics concepts to account for the fatigue crack growth process. This approach adopts the Paris equation [30], which relates the crack growth per cycle, *da/dN*, to the stress intensity factor range, $\Delta K$

$$\frac{da}{dN} = C\Delta K^m \qquad (1)$$

where $C$ and $m$ are material scaling constants that can be determined experimentally. $\Delta K$ can be calculated from the applied stress range ($\Delta\sigma$), crack size ($a$), and a geometry function ($f$)

$$\Delta K = f\Delta\sigma\sqrt{\pi a} \qquad (2)$$

Because Nitinol medical devices are geometrically small, fatigue crack growth is generally thought to comprise a small fraction of their life. Therefore, design has largely focused on prevention of crack initiation. While the total life approach remains the primary basis for assessing fatigue performance of medical devices, understanding and quantifying the effect of material discontinuities on the lifetime using the damage-tolerant approach should not be overlooked in the design process. However, considering the fundamental differences between the two approaches, extrapolating from one approach to another is not straightforward.

McCarver and Ritchie formulated a method to combine aspects of total life fatigue and damage-tolerant fatigue to investigate small crack growth thresholds in René 95 alloy [27,31]. Single edge notched bend (SENB) specimens were pre-cracked from a notch, where the notch was then removed through grinding to produce specimens with small edge cracks ranging from 10 to 200 μm. The specimens with these known small cracks were then fatigue tested at various stress amplitudes / stress intensity factor range ($\Delta K$) values until fracture or a runout of $5\times10^7$ cycles was achieved. The $\Delta K$ values were defined in terms of $\Delta K_i$ or initial stress intensity factor range, as the crack length was only known at the test start and not monitored. The threshold stress intensity factor range ($\Delta K_{th}$) value for small crack growth in this material was defined as the maximum $\Delta K_i$ value where no visible crack growth was observed, which according to the authors, "[is] a procedure analogous to the determination of a fatigue limit for S/N curves".

Before implementing McCarver and Ritchie's hybrid *S-N* technique to a medical device-size test specimen or component, the experimental techniques and assumptions would have to be modified. First, the specimens tested by McCarver and Ritchie were 6.35 mm thick, significantly larger than any structural element of a Nitinol vascular device, which are on the order of 100s of micrometers. Second, the fatigue-initiating feature on a Nitinol vascular medical device component would likely be a near-surface NMI, which are much smaller than the cracks tested in McCarver and Ritchie's study. To address these differences, both the test specimens and the starter cracks were scaled down in the present study. Nitinol wires with a diameter of 0.635 mm were used and FIB milling was employed to introduce starter cracks. The successful use of FIB milling to generate starter cracks has been reported in several studies [15,32–34].

Moreover, quantifying fatigue crack growth from an NMI-like discontinuity requires application of a stress intensity factor solution. The Murakami and Endo solution has been a well-established method to determine the stress intensity factor around an irregularly shaped small crack or an inclusion [35–37]. The solution proposes that the square root of the small crack area ($\sqrt{area}$) projected in the direction of the applied remote tensile stress ($\sigma$) is a promising representative dimension for small cracks and discontinuities. Murakami and Endo's stress intensity factor solution is:

$$K_{I_{max}} = 0.65\sigma\sqrt{\pi\sqrt{area}} \qquad (3)$$

$K_{I_{max}}$ is the Mode I maximum stress intensity factor along a three-dimensional crack. In the context of cyclic loading, Murakami and Endo's solution has previously been used with $\Delta K$ for fatigue analysis [32,34]. We used the modified Murakami and Endo solution in the present work to calculate the initial (subscript i) stress intensity factor range ($\Delta K_i$) using the initial crack area generated by FIB milling ($area_i$)

and the applied remote stress range ($\Delta\sigma$):

$$\Delta K_i = 0.65\Delta\sigma\sqrt{\pi\sqrt{area_i}} \qquad (4)$$

It is worth noting that a FIB-milled starter crack in a wire can also be viewed as a semi-elliptical crack in a rod under tension. Other researchers have shown that many semi-elliptical crack stress intensity factor solutions for a rod in tension become equivalent at small-crack penetration depths ($a/D$) including Murakami and Endo's solution [38,39]. Therefore, other solutions, such as Newman-Raju [40], may be used to calculate $\Delta K$ to within an acceptable deviation. For the purposes of our study, the use of Murakami and Endo's solution was preferred given its contextual use history around small cracks and NMIs.

In applying this solution, small-scale yielding (SSY) conditions are assumed, which are a prerequisite for the validity of linear elastic fracture mechanics (LEFM). As shown in several studies [41–44], the crack tip inelastic deformation zone, *i.e.*, the zone of phase transformation, martensite (re)orientation and/or plasticity in Nitinol, can be comparable in size to the characteristic dimensions of the crack configuration, and therefore LEFM requirements may not be met. In such cases, employing the *J*-integral, developed based on nonlinear-elastic fracture mechanics (NEFM), would relax such requirements. The use of *J*-integral or *J* (in overload fracture under monotonic mechanical loading) or cyclic *J*-integral or $\Delta J$ (in fatigue crack growth under thermomechanical cycling) is inevitable for a nonlinear, phase transforming material like Nitinol. However, at low mechanical load levels, such as those near fatigue thresholds, the inelastic component of $\Delta J$ becomes virtually zero ($\Delta J = \Delta J^{el}$) due to the insignificant nonlinearity in the response, such that the data can be described by $\Delta K$ [45].

## 3. Methods

### 3.1. Material

A high-purity vacuum arc remelted (HP-VAR) Nitinol wire (50.8 % at. Ni) produced by Confluent Medical (Fremont, California) was drawn, straightened, and centerless ground to create a bright surface finish with a final diameter of 0.635 mm and 40 % nominally retained cold work. Approximately 50 mm-long sections were cut from the spool for use as specimens for fatigue testing.

Differential scanning calorimetry (DSC) was performed in accordance with ASTM F2004 [46] to measure the transformation temperatures of the material. The austenite finish temperature, or $A_f$, measured
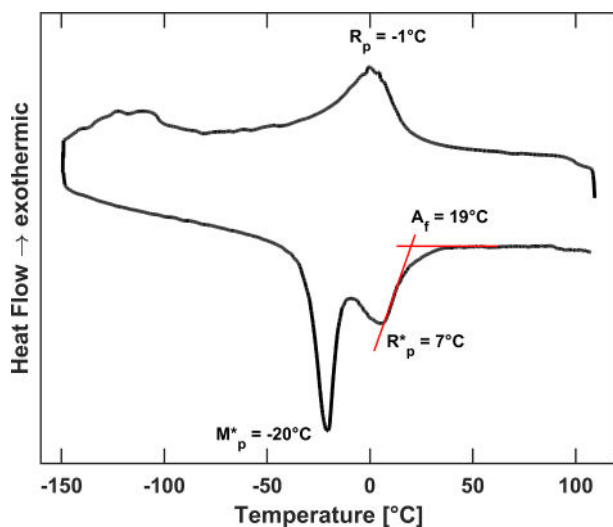
by DSC was 19 °C. Martensite and *R*-phase reversion peaks, *M\** and *R\** respectively, can be observed in the DSC trace of Fig. 1.

Quantification of the size and distribution of NMIs, particle-void assemblies (PVAs), and 'stringers' was performed on longitudinal and transverse wire cross sections. Wires were first potted in Buehler (Lake Bluff, Illinois) EpoThin 2 epoxy and allowed to cure for at least 12 hours before cross sectioning. The epoxy-mounted samples were then ground using silicon carbide papers with a final silicon carbide paper of 1200 grit. Samples were then polished using 3 μm and 1 μm diamond polishing suspensions followed by a final step using 0.05 μm alumina suspension. All polishing steps were performed on a Buehler AutoMet 250 with contra rotation of the head enabled.

The cross section and polished (unetched) samples were imaged at 1000x magnification on a Leica (Heerbrugg, Switzerland) DMI 5000 M metallographic microscope fitted with a Leica DFC450 digital microscope camera. The pixel resolution of the images from the metallograph at 1000x magnification were 0.0541 μm. The total area surveyed for each longitudinal and transverse cross section was 0.57 mm². The images were processed using a custom MATLAB script for detecting inclusions/porosity using image analysis, performing statistical analysis, and plotting the data. For inclusion detection image analysis, the MATLAB script utilized the "adaptthresh" command with a threshold set to 0.55 (scale range 0 to 1). Detected inclusions were encircled in red by the MATLAB script for each processed metallographic image. An example longitudinal metallographic image before and after inclusion detection can be observed in Fig. 2. The images were manually checked to ensure that the threshold value for detection was set accurately. The following inclusion metrics were calculated:

- $L_{max}$ = maximum inclusion length
- $L_{mean}$ = mean inclusion length
- $L_{median}$ = median inclusion length
- Total = total area fraction of measured inclusions in percent
- NMI Density = total number of inclusions divided by the total area surveyed

### 3.2. FIB milling of starter cracks

FIB was used to mill starter cracks of known dimensions into the wire fatigue specimens. Specimens were milled at the middle of the wire length using a FEI Versa 3D DualBeam (now Thermo Fisher Scientific, Waltham, Massachusetts) microscope. A 30 keV Ga + ion beam at 0.5 nA was used for the milling process and several starter crack sizes were milled for fatigue testing. The depth of the starter crack, or *a*, was kept consistent across all specimens at approximately 5.6 μm (<1% of the wire diameter). Several different crack widths, or *b*, were milled into the wires. The width sizes milled were 20, 25, 30, and 35 μm (3–6 % of the wire diameter). A small height, or *h*, of 0.5 μm was also milled to reach the desired milling depth. A representative starter crack on the wire surface after FIB milling can be observed in Fig. 3.

Preliminary FIB milling of starter cracks and subsequent FIB trench cross sectioning of those milled features revealed that the maximum achievable milling depth was approximately 5.6 μm when using a height of 0.5 μm. Trench cross sectioning of a FIB-milled starter crack can be observed in Fig. 4. At these dimensions, the FIB depth is limited by subsequent redeposition due to the aspect ratio ($a/h$) of the starter crack. To achieve greater milling depths, the milling height would need to increase to allow for exit of the sputtered material.

As shown in the cross-sectional view in Fig. 4, the FIB-milled starter cracks taper from their opening to a point at their final milled depth. FIB-milled features do not produce atomically sharp cracks since there is likely a small radius at the tip of the milled feature. However, an atomically sharp crack is expected to form once cyclic loading is initiated.
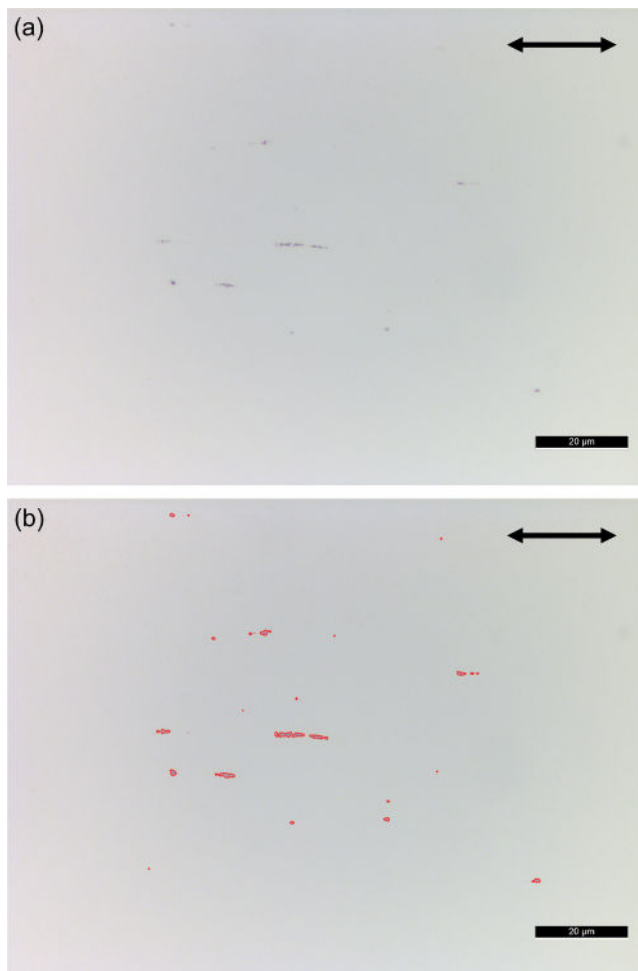


**Fig. 1.** Differential scanning calorimetry (DSC) trace of the Nitinol wire (50.8% at. Ni).

**Fig. 2.** Example longitudinal metallograph images from our cross sectioned and polished wires before (a) and after (b) inclusion detection from the custom MATLAB script. The detected inclusions are encircled in red (b). The black arrows indicate the wire drawing direction. (For interpretation of the references to colour in this figure legend, the reader is referred to the web version of this article.)
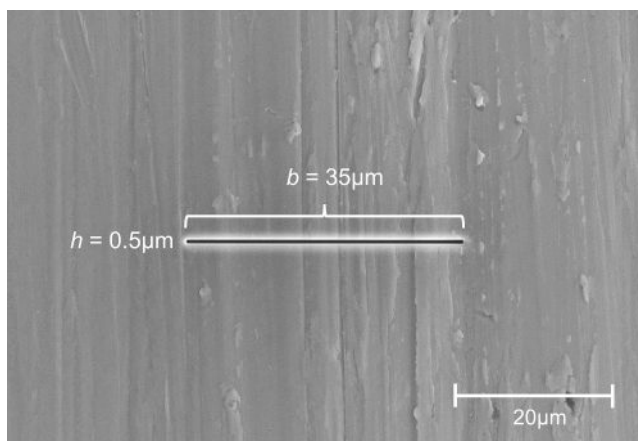


**Fig. 3.** A representative secondary electron micrograph of a FIB-milled starter crack looking at the top dead center of the wire surface with $b = 35$ μm and $h = 0.5$ μm.



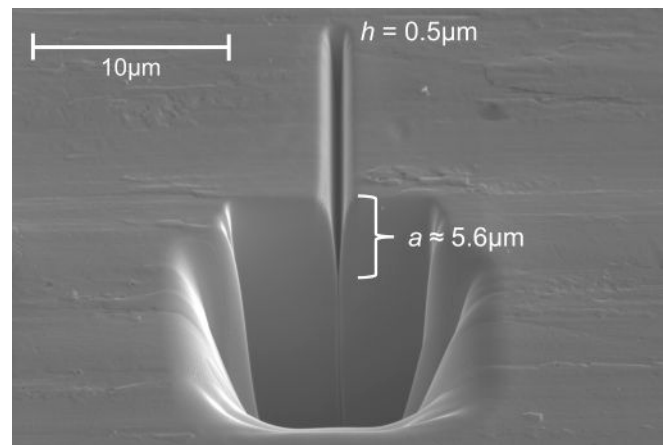**Fig. 4.** Secondary electron micrograph of a FIB-milled trench cross section of a FIB-milled starter crack with $b = 20$ μm. The FIB-milled starter crack tapers to a final point when milling and ion redeposition reach an equilibrium point. The line running down the tip of the starter crack is a curtaining artifact of FIB milling the trench cross section.

### 3.3. Fatigue testing

FIB-milled wire specimens were axial tension–tension fatigue tested on a TA Instruments (formerly Bose, New Castle, Delaware) Electroforce 3330 multi-specimen fatigue tester that had been retrofitted for single specimen use. Tension-tension fatigue testing was performed in ambient air at approximately 23 °C in a temperature-controlled room. The test temperature was above the measured $A_f$ ensuring that the material was tested in a superelastic condition. Custom fixtures were fabricated to grip the wire ends using 1/32 ER-16 collets. For testing, thin strips of 400-grit sandpaper were wrapped around the ends of the wire test specimens to promote friction at the grips during testing and to prevent damage to the specimens from the collet clamping force. One collet was attached to the machine actuator while the other collet was bolted onto an X-Y positioning stage attached to an 1100 N load cell. Specimens were gripped with a collet separation distance of approximately 25 mm.

Machine displacement to specimen strain correlation was performed on an Instron (Norwood, Massachusetts) 5982 Series load frame using the same fatigue test fixturing and wire specimens (no FIB milling). Wires were pulled at room temperature to 6 % strain and unloaded to correlate the machine displacements to specimen strain. A gauge length of 10 mm was used, and the engineering strain ($\Delta L/L_0$) was measured using the Instron video extensometer. The load was monitored using a 5 kN load cell. The machine displacement to strain data was analyzed using a MATLAB script to determine test settings. A representative stress–strain curve from correlation testing, loading to 6 % strain and then unloading back to zero, is shown in Fig. 5. The upper plateau and lower plateau stresses measured at room temperature were 490 and 290 MPa, respectively. It is clear from the stress–strain curve that superelasticity is present in our material at room temperature.

Fatigue tests were conducted to simulate a representative medical device load history with crimping into a catheter (6 % pre-strain), unloading into an undersized vessel (unload to 3 % mean strain), and cycling *off the lower plateau* (see Fig. 5) with representative biomechanical motions. This loading regime is well established in the Nitinol literature and is described in greater detail elsewhere [3,4,17].

The fatigue testing was conducted under displacement-control conditions at a cycling frequency of 20 Hz. Displacement-control is favored in total life fatigue testing due to the phase transforming nature of superelastic Nitinol. It is worth mentioning that depending on the cycling conditions, the specimen response can be nominally elastic, and the displacement-control becomes equivalent to load-control. This occurs when cyclic strain amplitudes remain within the hysteresis loop (*i.e.*
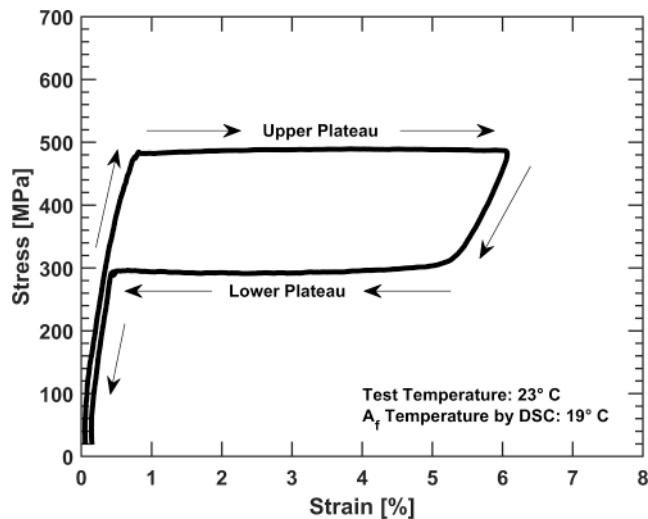
**Fig. 5.** A representative stress–strain curve from machine displacement to strain correlation testing.

between the upper and lower plateau). In such a condition, the material is non-phase-transforming, and the mixed-phase material undergoes a nominally elastic loading [17,47]. In our study, the phase-transformation occurs primarily during pre-straining and unloading to the mean strain condition. We discuss, in more detail, the nominally elastic cycling state of our material in Section 5.2.1.

Strain amplitudes were varied between 1.0 and 0.375 %. Six specimens were tested at each strain amplitude condition for each of the four different FIB-milled starter crack widths (24 total specimens tested at each strain amplitude). Specimens that fractured in the gauge length of 10 mm were considered valid test specimens and were confirmed by scanning electron microscopy (SEM) to have initiated at the FIB-milled starter crack. Specimens that failed at the grips were excluded from the data set.

The fatigue test data were analyzed in terms of strain amplitude, stress amplitude, and initial stress intensity factor range, $\Delta K_i$. For our study, we were able to use displacement-controlled fatigue testing methods to calculate stress values because our specimens were round wires with simple geometry. Stress amplitude was calculated from the following equation:

$$\sigma_a = \frac{P_{max} - P_{min}}{2 \times A} \tag{5}$$

where $P_{max}$ was the average max load over the test, $P_{min}$ was the average minimum load over the test, and $A$ was the original cross-sectional area of the wire. Note that the calculated stress amplitude was the stress in the far-field. No significant decay in the maximum or minimum loads were observed apart from specimen fracture during fatigue testing, thereby justifying the appropriateness of using average values. $\Delta K_i$ values were calculated using Equation (4). The square root area term in Equation (4) is the square root of the FIB stater crack area ($a \times b$).[1] Calculating the data in terms of $\Delta K_i$ is advantageous, as crack growth does not need to be monitored and we can treat $\Delta K_i$ as an *S-N* style parameter.

Lastly, all FIB-milled wire specimens that fractured in the gauge section during fatigue testing were examined under SEM using an FEI Versa 3D DualBeam microscope and a JEOL JSM-LV400 (Tokyo, Japan). Each fracture surface was imaged to identify the fracture origin, detail

the progression of crack growth until fracture, and measure the dimensions of the FIB-milled starter crack if it coincided with the fracture origin.

### 3.4. Statistical data analysis

Binomial logistic regression was performed on the fatigue data to determine the probability of fatigue fracture to elucidate fatigue limits and a small crack growth threshold or $\Delta K_{th,\ sc}$. The logistic regression was conducted in the same manner as outlined in Malito et al. and Robertson et al. [4,13]. The raw fatigue data were first converted to a binary data set by assigning values of 1 or 0 for a failure or runout event, respectively at the end test condition of $10^7$ cycles. The average probability for fatigue fracture at $10^7$ cycles was then calculated for strain amplitudes, stress amplitudes and $\Delta K_i$. For the stress amplitude and $\Delta K_i$ data, an added binning or grouping step was performed due to the spread in the data. The averaged data were then plotted as the probability of fatigue fracture *vs.* strain amplitude, stress amplitude, and $\Delta K_i$. A sigmoidal curve was fit to the data using the following logistic response function:

$$P = \frac{e^{x^T \beta}}{1 + e^{x^T \beta}} \tag{6}$$

where $P$ is the probability of fatigue fracture at $10^7$ cycles, $x$ is a vector of strain/stress amplitudes or $\Delta K_i$ values, and $\beta$ is a vector of model coefficients. Goodness of fit was assessed using Pearson's chi-squared ($\chi^2$) test. The binomial logistic regression and statistical analysis was performed using a custom MATLAB script.

## 4. Results

### 4.1. Inclusion distribution analysis

Histogram plots detailing the results of the inclusion distribution analysis for the longitudinal and transverse cross sections can be observed in Fig. 6. The superimposed histogram plots compare the distribution of the area fraction of inclusions as well as the number of inclusions *vs.* inclusion length. Table 1 lists the important metrics from the inclusion distribution analysis. The $L_{max}$ values observed for the longitudinal and transverse cross sections were approximately 9 and 2 μm, respectively. The $L_{median}$ values for the longitudinal and transverse cross sections were less than the $L_{mean}$ values, signifying that the inclusion distribution length measurements were skewed right as evidenced by the histograms in Fig. 6. Overall, the inclusion distribution analysis demonstrated that the native inclusions in the transverse direction of the wire were smaller than the FIB starter cracks milled into the wires for fatigue testing. Therefore, the FIB-milled starter cracks were expected to be the dominating feature for the initiation and propagation of small cracks during fatigue testing.

### 4.2. Fatigue testing

In total, 129 wire specimens were axial tension–tension fatigue tested after tension pre-straining to 6 % and unloading to a mean strain of 3 % before cycling. Twenty-four specimens were tested in each of five strain amplitude values between 0.875 and 0.375 % in 0.125 % increments. Only nine specimens were tested in the low-cycle condition of 1.0 % strain amplitude due to i) the consistent low-cycle fatigue behavior under this condition, and ii) the propensity of fracture initiation outside of the gauge section.

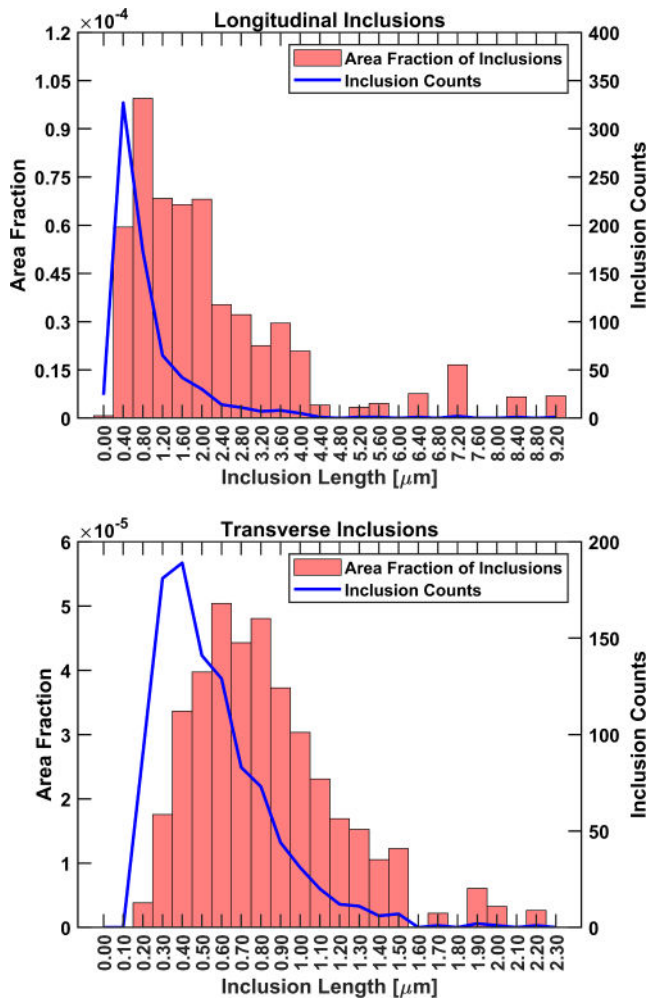From the 129 specimens tested, nine specimens fractured in the

---

[1] Although described earlier as a semi-elliptical crack, we adopted a simple rectangular area calculation approximation as justified by the projected area of these micro-milled features observed post-fracture (Figs. 12-13).

**Fig. 6.** Histogram plots of the area fraction size and number of inclusions for the longitudinal (top) and transverse (bottom) Nitinol wire cross sections surveyed over a 0.57 mm² area.

**Table 1**

Inclusion distribution analysis metrics for the Nitinol wire cross sections with an area survey of 0.57 mm² for longitudinal and transverse orientation.

| Orientation | $L_{max}$ [μm] | $L_{mean}$ [μm] | $L_{median}$ [μm] | Total [%][a] | NMI Density [#/mm²] |
|---|---|---|---|---|---|
| Longitudinal | 9 | 0.92 | 0.6 | 0.06 | 1247 |
| Transverse | 2 | 0.55 | 0.49 | 0.04 | 1785 |

[a] These area percentage values are lower than the reported values from the raw 12.7 mm (0.5 in) bar used to manufacture the wire used in this study. It is possible that higher magnification imaging (greater than 1000X) is required to survey inclusions for final drawn HP VAR Nitinol material. Understanding the scope and limitations of surveying inclusions in these high purity Nitinol materials is beyond the current study and would require further investigation.

gauge section with fatigue fracture initiating elsewhere from the FIB starter crack, 77 specimens[2] fractured in the gauge section with fracture originating from the FIB stater crack, and 43 specimens ran out to $10^7$ cycles. An image of a specimen that fractured in the gauge section with initiation at the FIB starter crack can be observed in Fig. 7.

---

[2] One specimen was excluded from the $\Delta K_i$ data set because of an inconclusive fracture initiation site due to post-fracture smearing.



**Fig. 7.** Image of a FIB-milled wire test specimen that had fractured from the gauge section under axial tension–tension fatigue. The fracture had originated at the FIB-milled starter crack. The specimen depicted in the image fractured at 4.22 million cycles.

### 4.2.1. Strain amplitude lifetime S-N curves

Axial tension–tension fatigue test results for strain amplitude can be observed in Fig. 8. The fatigue plot exhibits the bimodal trend commonly observed in Nitinol fatigue testing, where an abrupt change between low-cycle and high-cycle fatigue occurs with relatively few high-cycle fatigue failures. All specimens were observed to initiate fracture at the FIB starter crack, except those tested at 1.0 % strain amplitude, at which fatigue fracture originated elsewhere on the specimen. As mentioned previously and discussed in detail in Section 5.2.1, the total number of specimens tested at this amplitude was reduced due to the difficulty in
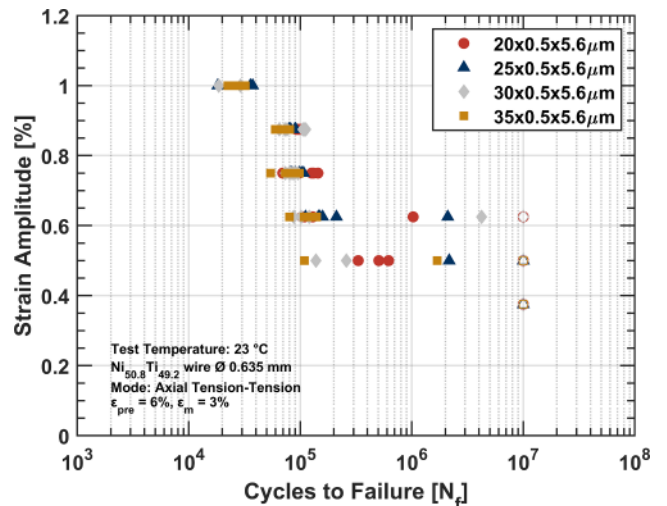


**Fig. 8.** Stain amplitude *vs.* cycles to failure (*S-N*) plot for all the axial tension–tension FIB-milled starter crack Nitinol wire specimens subjected to fatigue testing at 6% pre-strain and 3% mean strain conditions. Specimens were tested up to $10^7$ cycles. Filled markers represent specimen fractures while open markers represent specimen runouts.

obtaining specimen fractures within the gauge length. Wire specimens tested at 0.625 % and 0.5 % amplitude exhibited a mixture of fatigue fractures and runouts to $10^7$ cycles. Finally, all specimens tested at 0.375 % amplitude reached $10^7$ cycles without fracture.

#### 4.2.2. Stress amplitude lifetime S-N curves

Axial tension–tension fatigue test results in terms of stress amplitude are shown in Fig. 9. Although Nitinol fatigue data are not typically presented in terms of stress amplitude because of the non-linear nature of the material, it can provide valuable insights in this case given the tension–tension testing conditions and the simplified wire specimen geometry.

Comparing the strain and stress amplitude *S-N* curves, the stress amplitude plot exhibits much less data scatter. Correspondingly, a gap opens in the data, approximately between 110 and 100 MPa. The stress amplitude data above 110 MPa corresponds to the 1.0 % strain amplitude test condition. A 100 MPa stress amplitude represents the higher load spectrum of specimens tested at 0.875 % strain amplitude.

The load ratio ($R = \sigma_{min}/\sigma_{max}$) for the fatigue tests varied from 0.43 to 0.75. This variation is consistent with conducting displacement/strain control tests. Despite the varying load ratio, the mean stress was relatively consistent across all tests, with an average of 316 ± 17 MPa. The tested stress amplitudes ranged from 131 to 42 MPa. The highest stress amplitude where runout to $10^7$ cycles was observed was 77 MPa, corresponding to a 0.625 % strain amplitude. All the runouts from 0.375 % strain amplitude had a corresponding stress amplitude ranging from 53 to 42 MPa. All tested specimens were observed to runout to $10^7$ cycles at or below approximately 58 MPa.

#### 4.2.3. Initial stress intensity factor Range, $\Delta K_i$

The axial tension–tension fatigue test results in terms of $\Delta K_i$ *vs.* cycles to failure are shown in Fig. 10. The results are from specimens that exhibited fatigue fracture initiating at a FIB-milled starter crack or reached $10^7$ cycles. Moving from stress amplitude (Fig. 9) to $\Delta K_i$ (Fig. 10), a further reduction in data scatter is observed. This reduction is most likely due to the loading parameter being further normalized by applying the stress intensity factor solution, Equation (4). To this aim, the area dimensions of each FIB starter crack were measured in the SEM for each fractured specimen and then applied to the specific specimen data point. For runout specimens, an average *b* and *a* was calculated from each FIB starter crack width group (20, 25, 30, and 35 μm) to
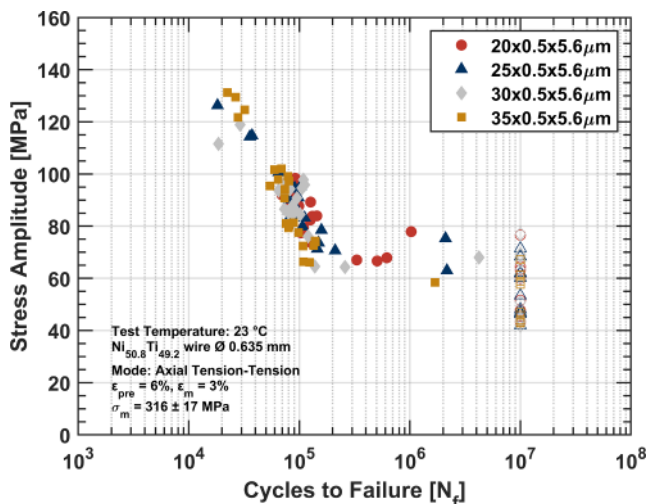


**Fig. 9.** Stress amplitude *vs.* cycles to failure (*S-N*) plot for all the axial tension–tension FIB-milled starter crack Nitinol wire specimens subjected to fatigue testing at 6% pre-strain and 3% mean strain conditions. Specimens were tested up to $10^7$ cycles. Filled markers represent specimen fractures while open markers represent specimen runouts.
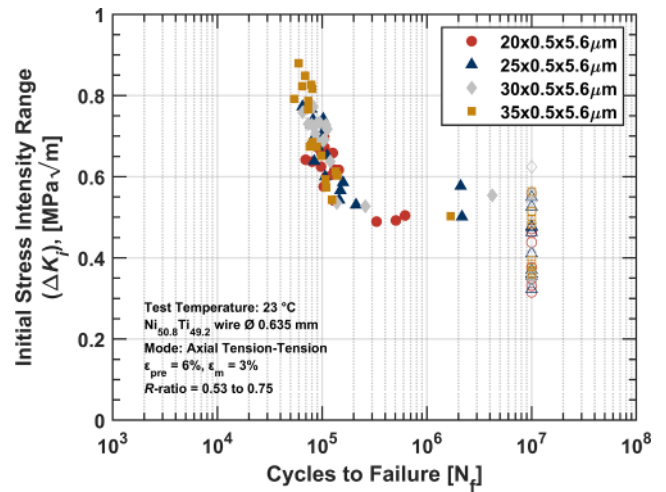


**Fig. 10.** Initial stress intensity factor range ($\Delta K_i$) *vs.* cycles to failure plot for the axial tension–tension FIB-milled starter crack Nitinol wire specimens subjected to fatigue testing at 6% pre-strain and 3% mean strain conditions that fractured at a FIB starter crack. Specimens were tested up to $10^7$ cycles. Filled markers represent specimen fractures while open markers represent specimen runouts.

calculate $\Delta K_i$.

The data in Fig. 10 are from the strain amplitude tests run at or below 0.875 % amplitude or 100 MPa stress amplitude since those tests all produced fatigue fractures starting at the FIB starter crack or runout. The calculated $\Delta K_i$ values ranged from 0.88 to 0.32 MPa$\sqrt{\text{m}}$. The highest $\Delta K_i$ where runout to $10^7$ cycles was observed was 0.62 MPa$\sqrt{\text{m}}$ for a 30 μm wide FIB starter crack specimen, corresponding to 0.625 % strain and 77 MPa stress amplitude. All tested specimens were observed to runout to $10^7$ cycles at or below approximately 0.48 MPa$\sqrt{\text{m}}$.

#### 4.3. Statistical data analysis

The fitted sigmoidal logistic regression curves for the $10^7$-cycle probability of fatigue fracture at different strain amplitudes, stress amplitudes, and $\Delta K_i$ values are presented in Fig. 11 a, b, and c, respectively. Table 2 lists the results for the median and 95 % lower bound (LB) (95 % confidence) probability of fatigue fracture at 50 %, 10 %, 5 %, and 1 % for the three parameters. Overall, at 50 % probability of fatigue fracture, there is little difference between the expected values and 95 % LB values across all conditions. Going to lower probabilities, especially for the 5 % and 1 % cases, a larger difference between the expected values and 95 % LB values arose, as demonstrated in Fig. 11.

As mentioned previously, all specimens ran out to $10^7$ cycles at or below 0.375 % strain amplitude, 58 MPa stress amplitude, or a $\Delta K_i$ of 0.48 MPa$\sqrt{\text{m}}$. When comparing these values with our statistical analysis, these observed test runout conditions carried some inherent probability of fatigue fracture. For a 0.375 % strain amplitude, our analysis would predict an expected value and 95 % LB probability of fatigue fracture of 1.8 % and 9.1 %, respectively. For a 58 MPa stress amplitude, our analysis would predict an expected value and 95 % LB probability of fatigue fracture of 11 % and 29 %, respectively. Finally, for a $\Delta K_i$ of 0.48 MPa$\sqrt{\text{m}}$, our analysis would predict an expected value and 95 % LB probability of fatigue fracture of 20 % and 41 %, respectively.

The *p*-values for the logistic regression model coefficients, $\beta$, across strain amplitude, stress amplitude, and $\Delta K_i$ curves were all less than 1 × $10^{-5}$. The low *p*-values for the model coefficients demonstrate the high goodness of fit of the sigmoidal curves to the fatigue test data. The goodness of fit is most likely due to the large number of tested and runout specimens generated for the data set. The high degree of fit can also be observed by how close the 95 % LB is to the median sigmoidal curve across the three conditions in Fig. 11. The Pearson residuals fit a
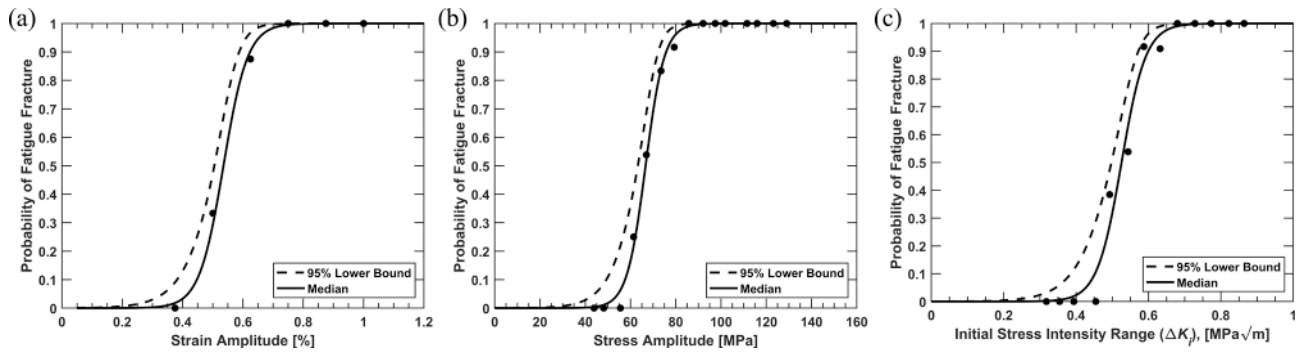
**Fig. 11.** Sigmoidal logistic regression curves showing probability of fatigue fracture *vs.* (a) strain amplitude, (b) stress amplitude, and (c) $\Delta K_i$ at $10^7$ cycles. The solid line represents the median fit to the data and the dashed line represents the 95% lower bound to the fitted data.

**Table 2**
Selected probability of fatigue fracture at $10^7$ cycles for strain amplitude, stress amplitude, and $\Delta K_i$. Median probabilities as well as the 95% lower bound (LB) results are listed.

| Probability of Fatigue Fracture at $10^7$ Cycles [%] | Strain Amp. [%] | 95 % LB Strain Amp. [%] | Stress Amp. [MPa] | 95 % LB Stress Amp. [MPa] | $\Delta K_i$ [MPa$\sqrt{m}$] | 95 % LB $\Delta K_i$ [MPa$\sqrt{m}$] |
|---|---|---|---|---|---|---|
| 50 | 0.54 | 0.51 | 67 | 64 | 0.53 | 0.50 |
| 10 | 0.45 | 0.39 | 58 | 50 | 0.45 | 0.39 |
| 5 | 0.42 | 0.34 | 55 | 45 | 0.43 | 0.34 |
| 1 | 0.35 | 0.23 | 48 | 33 | 0.37 | 0.25 |

normal distribution for the strain amplitude, stress amplitude, and $\Delta K_i$ logistic regression curves. The Pearson's $\chi^2$ test is most accurate for the stress amplitude, and $\Delta K_i$ sigmoidal curve fits due to the number of data points that were binned for the curve fit. Comparatively, the Pearson's $\chi^2$ is less accurate for the strain amplitude logistic regression fit as only six strain amplitudes were tested and therefore binned for analysis.

### 4.4. Fatigue limits and small crack growth threshold

The statistical analysis presented in the previous section provides useful insight into elucidating both stress and strain amplitude endurance/fatigue limits for this Nitinol material under axial tension–tension loading. Based on the more conservative definition of the fatigue limit ($S_f$) provided in ASTM E1823 [48] we have defined our tension–tension fatigue limits to be the 5 % probability of fatigue fracture (*i.e.*, 95 % survival) at $10^7$ cycles and 95 % confidence (*i.e.*, 95 % lower bound).

The tension–tension alternating strain and stress fatigue limits ($\varepsilon_{f,a}$ and $\sigma_{f,a}$) at $10^7$ cycles, along with associated test conditions such as pre-strain, mean strain, and mean stress are listed in Table 3. The values in Table 3 are taken from the results of the probability analysis shown and tabulated in Fig. 11 and Table 2.

The same fatigue limit analysis can be applied to the $\Delta K_i$ data to determine a small crack growth threshold or $\Delta K_{th,sc}$. Correspondingly,

**Table 3**
Fatigue limit (strain and stress) and the small crack growth threshold of our Nitinol material at $10^7$ cycles. As a reminder, the fatigue limits and small crack growth threshold listed here are from axial tension–tension fatigue tests with the presence of a FIB-milled starter crack. Finally, the strain and stress-based fatigue limits are not from crack-tip stresses but from the far-field strain/stresses in the wire.

| Test Parameter | Limit/Threshold | Loading Conditions |
|---|---|---|
| Strain | $\varepsilon_{f,a} = 0.34$ % | $\varepsilon_{pre} = 6$ %, $\varepsilon_m = 3$ % |
| Stress | $\sigma_{f,a} = 45$ MPa | $\varepsilon_{pre} = 6$ %, $\varepsilon_m = 3$ %, $\sigma_m = 316$ MPa |
| $\Delta K_i$ | $\Delta K_{th,sc} = 0.34$ MPa$\sqrt{m}$ | $\varepsilon_{pre} = 6$ %, $\varepsilon_m = 3$ %, $R = 0.75$ |

the $\Delta K_{th,sc}$ for our material is listed in Table 3 along with associated test parameters.

### 4.5. Fractography

In total, 86 specimens fractured in the gauge section during testing and were subsequently investigated with SEM to measure the dimensions of the starter cracks and examine fractographic features. Of the 86 fractured specimens, 77 specimens fractured at the FIB-milled starter crack.

Fractography allowed for the examination and quantification of two main aspects of the fractured specimens: (i) measurement of the initial dimensions of the FIB-milled starter cracks; (ii) assessment of relevant Nitinol fractographic features such as the presence of fatigue striations, "feathering lines", microvoid coalescence, and semi-elliptical crack growth.

#### 4.5.1. FIB starter crack quantification

All 77 specimens with fractures initiating at FIB starter cracks were physically measured via SEM from their corresponding fracture surfaces. This method enabled accurate determination of $\Delta K_i$ for each individual fractured specimen compared to using nominal values. This also allowed for tabulation of the average *a* (*i.e.*, milling depth) and average *b* (*i.e.*, milling width) for our four types of FIB starter cracks.

The average dimensions of the FIB-milled starter cracks from 76 fractured specimens are listed in Table 4. During the fracture surface examination, one specimen had an inconclusive fracture initiation site due to post-fracture smearing. As a result, this specimen was not included for FIB-milled starter crack measurement. The average *a* was consistent across the four starter crack groups at approximately 4.82 to 4.89 μm. The average values listed in Table 4 were the FIB-milled starter crack values used to compute $\Delta K_i$ for the specimens that reached $10^7$ cycle runout.

#### 4.5.2. Fractographic features

The fracture surface from a 20 μm wide FIB starter crack specimen tested at 0.5 % strain amplitude and 3 % mean strain is shown in Fig. 12. As show in Fig. 12 a, the remnants of a semi-elliptical crack front were observed from the origin at the top of the figure. Crack growth extended approximately 40 % across the wire diameter before final fracture. At higher magnification (Fig. 12 b), the fracture origin was confirmed to be

**Table 4**
Crack dimensions measured from the 76 specimens where fracture originated from the FIB-milled starter crack that could be imaged.

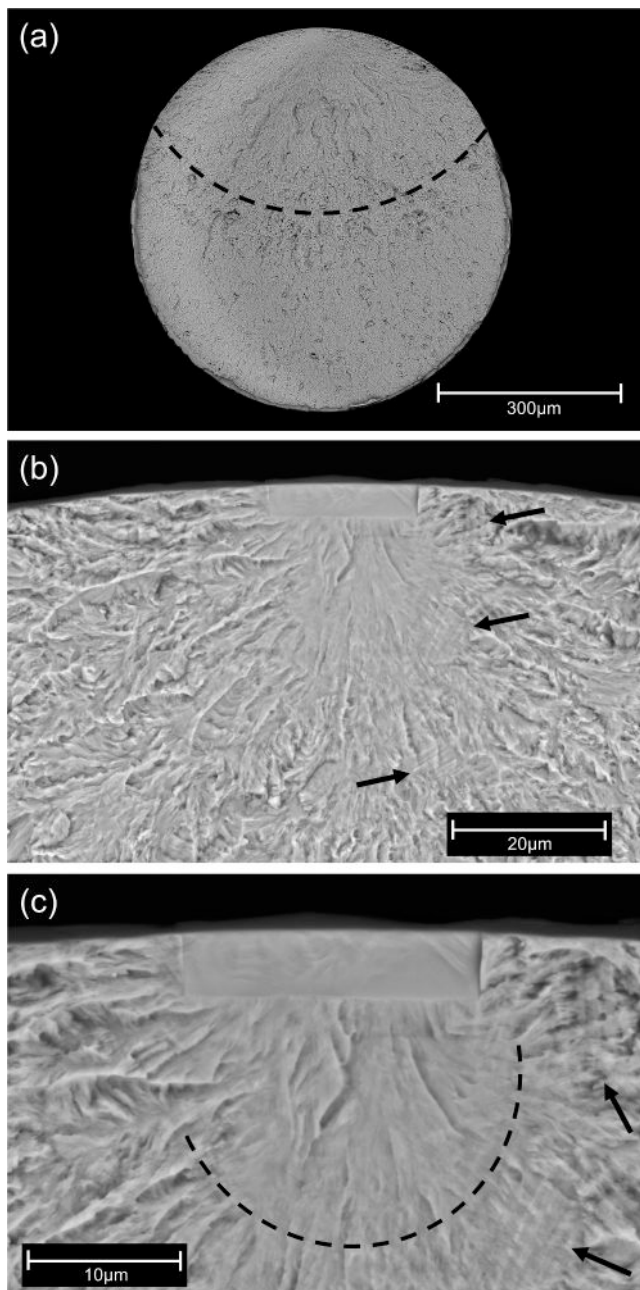| | Nominal FIB Starter Crack Widths | | | |
|---|---|---|---|---|
| | 20 | 25 | 30 | 35 |
| *b* (μm) | 20.73 ± 0.84 | 25.51 ± 0.78 | 31.37 ± 1.17 | 36.50 ± 1.29 |
| *a* (μm) | 4.87 ± 0.54 | 4.86 ± 0.39 | 4.89 ± 0.77 | 4.82 ± 0.40 |

**Fig. 12.** Back scatter electron (BSE) micrographs of the fracture surface from a 20 μm wide FIB starter crack specimen tested at 0.5 % strain amplitude. (a) Overview of the fracture surface where a semi-elliptical crack front can be observed. (b) Higher-magnification image of the FIB-milled starter crack as the fracture origin. Black arrows highlight the presence of multiple sets of fatigue striations. (c) Higher magnification BSE micrograph of semi-elliptical crack growth close to the FIB starter crack. The black arrows point to fatigue striations associated with the semi-elliptical crack front.



**Fig. 13.** BSE micrographs of the fracture surface from a 20 μm FIB starter crack specimen tested at 0.75 % strain amplitude. (a) overview of the fracture surface where a semi-elliptical crack front can be observed transitioning into the overload region. (b) higher-magnification image of the FIB-milled starter crack as the fracture origin. Black arrows highlight the presence of a set of fatigue striations emanating directly from the FIB-milled starter crack. (c) Higher magnification BSE micrograph of the fracture origin where fatigue striations are observed emanating directly from the corner of the FIB-milled starter crack.

the FIB-milled starter crack. Additionally, several distinct fractographic features were present. "Feathering lines" were observed emanating from the FIB-milled starter crack origin along with several groups of fatigue striations on the fracture surface (black arrows Fig. 12 b). Evidence of semi-elliptical crack (Fig. 12 c) growth very close to the FIB starter crack was also observed. Two groups of fatigue striations were connected to the semi-elliptical crack front near the FIB starter crack.

The fracture surface from a 20 μm wide FIB starter crack specimen tested at 0.75 % strain amplitude and 3 % mean strain is shown in Fig. 13. Consistent with the specimen shown in Fig. 12, a well-defined
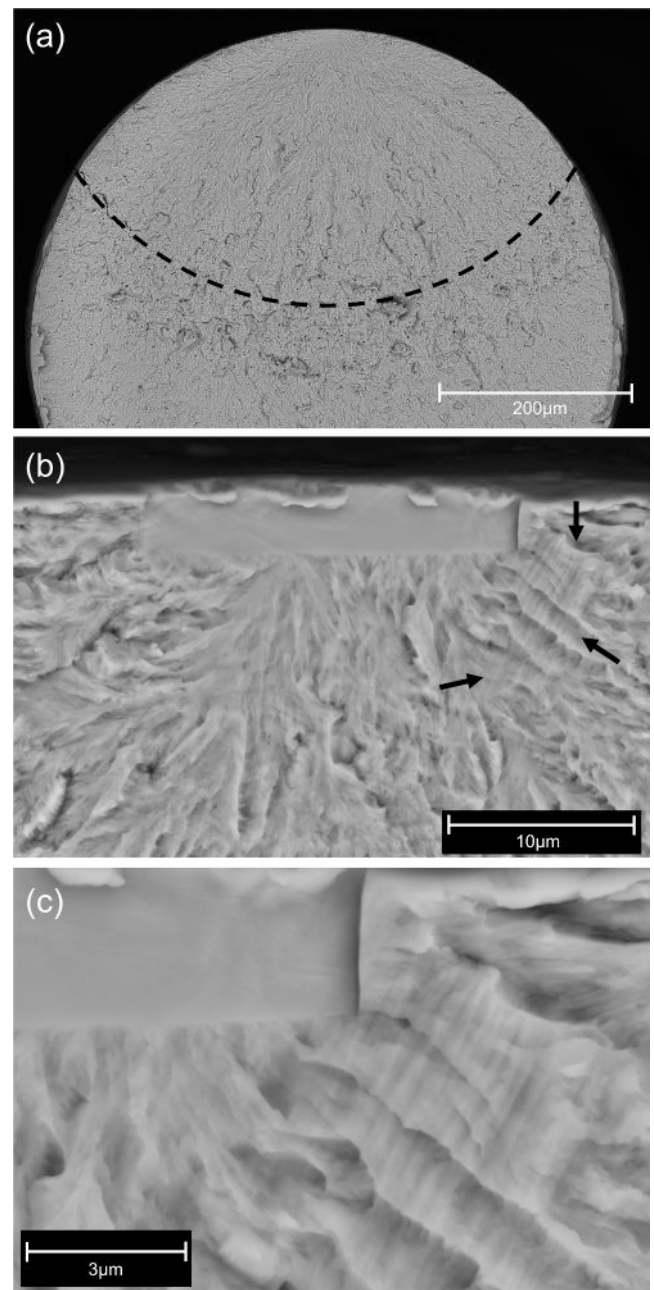
semi-elliptical crack front was present, with "feathering lines" pointing back to an origin at the top of the image. At higher magnification, the fracture origin is confirmed as the FIB-milled starter crack. Fatigue striations emanate directly from the corner of the FIB-milled starter crack (Fig. 13 b,c). It is possible that similar striations were present at one point at the FIB-milled starter crack in Fig. 12 but were damaged or worn during further cycling.

## 5. Discussion

To the authors' knowledge, the present study is the first attempt to determine the $\Delta K_{th,sc}$ for superelastic Nitinol using fabricated small cracks and in specimen geometries (<1mm) relevant to those commonly employed in medical devices. We calculated this critical material parameter through axial tension–tension fatigue testing of Nitinol wires using a hybrid *S-N* and fracture mechanics-based approach. Other studies have attempted to calculate $\Delta K_{th,sc}$ from either long crack growth data [22], from fatigue cracks initiating from near surface NMIs [16], or deduced from the combination of material hardness and initiating inclusion size [18]. Our study was able to control for most of the experimental conditions that these studies were not able to, including:

1. Relevant fracture mechanics Mode I axial tension–tension loading conditions.
2. Precise starter cracks via FIB at size scales greater than inherent NMIs in the material.
3. Size scales and strain loading conditions (cycling from the lower plateau after a relevant pre-strain) relevant to Nitinol medical devices.
4. Sufficiently large sample population for relevant statistical analysis.

In addition, our study calculated an applicable stress-based fatigue limit, which is often overlooked in the structural fatigue of Nitinol. Given Nitinol's non-linear mechanical behavior, structural fatigue parameters are typically reported in terms of strain [14]. In our study, we examined Nitinol fatigue in terms of stress given the simplified specimen geometry, the axial tension–tension loading conditions, and derived a tension–tension stress-based fatigue limit for Nitinol relevant to medical device applications. The stress-based fatigue limit was derived from cycling fully from the lower plateau and after exposure to a relevant pre-strain.

### 5.1. Fatigue limit

#### 5.1.1. Rationale for fatigue limit

ASTM E1823 defines the standard terminology related to fatigue and fracture testing and lists two definitions for fatigue limit [48]:

1. "the limiting value of the median fatigue strength as the fatigue life, $N_f$, becomes very large", and
2. "the limiting value of fatigue strength for *p* % survival as *N* becomes very large; *p* may be any number, such as 95, 90, and so forth."

Both definitions provided by ASTM E1823 do not eliminate the possibility of fracture. The first definition states 50 % of the specimens are predicted to fracture (*i.e.*, 50 % survival) at the defined fatigue limit. This definition may not be suitable for certain critical engineering applications. The second definition is more conservative, as it includes the probability for specimen failure to be quite low, such as 5 or 10 % (*i.e.*, 95 or 90 % survival, respectively). The second definition is more appropriate for use in safety critical engineering applications like those of implantable medical devices.

Both definitions state that the cycle count must become "very large", but they do not list a cycle count for which a fatigue limit must be derived. As a result, the fatigue limit should be defined at the highest cycle count/runout condition physically tested to avoid ambiguity or false predictions, *i.e.*, there should be no extrapolation beyond the tested cycle count.

As mentioned in the results section, we have chosen a more stringent definition of the fatigue limit outlined by ASTM E1823, allowing for a 5 % probability of fatigue fracture (*i.e.*, 95 % survival) at 95 % confidence (*i.e.*, 95 % lower bound). This is in line with the general safety critical practices used by medical device manufacturers when fatigue testing Nitinol devices.

#### 5.1.2. Strain-Based axial Tension-Tension fatigue limit

The axial tension–tension fatigue data of high-purity (HP VAR) superelastic Nitinol wire has been previously published by Robertson et al. [4]. The reported strain-based fatigue limit was 0.32 % at $10^7$ cycles, which is lower than the fatigue limit reported in the present study for wires with FIB-milled starter cracks. This difference could stem from several factors that are briefly discussed below.

Variations in the underlying microstructure from lot-to-lot is one likely contributor to the differences observed between our study and the earlier Robertson et al. paper [4]. Specifically, the inclusion content of the wires utilized in this current study was particularly superior to that in the previous study, thereby minimizing intrinsic failure mechanisms. Comparing our inclusion distribution analysis results to those reported by Robertson et al., the abundance of inclusions is ∼ 7X less and the size is ∼ 4X less in the current wires. Because the probability of containing a larger inclusion, which thereby increases the localized stress concentration in the initiation zone, it is unsurprising that the Robertson et al wires exhibited a diminished durability relative to the wires studied herein. These marked differences in inclusion distribution do not, however, reconcile why laboratory-induced extrinsic defects larger than the intrinsic features in the current study still produced superior fatigue durability.

The Nitinol wire material that was investigated by Robertson et al. had also undergone different processing conditions resulting in differences in the wire mechanical behavior and microstructure. Particularly, the HP VAR material in Robertson et al. was heat treated (505 °C for 2–5 min) after cold working and wire straightening while our material was not exposed to any post cold work and post straightening heat treatments. As can be seen from the DSC (Fig. 1) and stress–strain (Fig. 5) curves our material's behavior was heavily influenced by the presence of *R*-phase. The presence of *R*-phase can lead to improved strain-based fatigue performance since it is more compliant than austenite and therefore has a greater elastic range [17]. Moreover, the HP VAR Nitinol wires in Robertson et al. were chemically etched and polished after heat treatment to remove the oxide, create a smooth surface, and produce a reduced section in the wire diameter. Our wires were centerless ground to remove the oxide surface from the drawing process with no post chemical treatment. Centerless grinding combined with the drawing process would leave some compressive residual stresses on the wire. Furthermore, residual beneficial compressive stresses at the root of the FIB-milled starter crack cannot be ruled out. Residual stresses would most likely have been removed in the wires from Robertson et al. from the heat treatment and the chemical surface processing, leading to some differences in fatigue performance.

#### 5.1.3. Stress-Based axial Tension-Tension fatigue limit

The stress-based tension–tension fatigue limit of superelastic Nitinol has been previously reported in a few studies [14,17,19,22,49,50]. These studies include fatigue investigations performed on Nitinol tubing, reduced section wires, and sheet. The runout conditions for these various studies were mainly limited to $10^6$ and $1.5 \times 10^6$ cycles. Only Launey et al. had a similar runout condition to our study of $10^7$ cycles. These fatigue studies list a wide range for stress-based fatigue limits from 600 MPa to 50 MPa stress amplitude.

In our study, all FIB-milled wire specimens were observed to run out at or below a stress amplitude of 58 MPa at $10^7$ cycles. Also, our stress-based fatigue limit derived from logistic regression curves with a 5 % probability of fatigue fracture (*i.e.*, 95 % survival) at $10^7$ cycles and 95 % confidence (*i.e.*, 95 % lower bound) was 45 MPa. The highest stress amplitude where all runouts occurred (58 MPa, *R*-ratio = 0.67) is towards the lower bound of the previously reported tension–tension fatigue limit of Nitinol. The statistically derived fatigue limit reported in the present study (45 MPa, *R*-ratio = 0.75) falls below the lower-bound tension–tension fatigue limit.

The difference observed in axial tension–tension fatigue limit characteristics can be attributed to the following. Firstly, our specimens

contained FIB-milled starter cracks which would most likely produce lower fatigue limits than smooth specimens. Second, our stress-based fatigue limit is determined from a significantly larger number of specimens, 129 in total, including 43 runout tests. Moreover, the runout test condition for our study was $10^7$ cycles (an order of magnitude difference with many of the previously mentioned studies), which can produce lower stress fatigue limits. Additionally, differences in material composition, thermomechanical processing, surface smoothness and specimen geometry can affect the fatigue properties of Nitinol [14]. For instance, variations in the plateau stresses were observed by Lopes et al. for the four different heat-treatment groups for the same resultant $A_f$ temperature. As a result, even though the same mean strain was achieved across tests, different mean stresses were tested for each heat-treatment condition. The stress-based fatigue limit of Nitinol could also be affected by mean stress and the resulting $R$-ratio [22,29]. Lastly, the difference in cycling location on the stress–strain curve is expected to affect the mechanisms of damage accumulation, and therefore, fatigue characteristics. For example, Alarcon et al. cycled the specimens in the region of austenite elasticity. Lopes et al. pre-strained the specimens to 6 %, unloaded them to 1.5 % strain and then cycled. While the specimens in the present study were loaded to the same pre-strain (6 %), the cyclic mean strain was higher at 3 %, typical for medical device applications.

As mentioned, mean stress and $R$-ratio can affect the stress-based fatigue limit of Nitinol, however, understanding such effects is challenging, mainly because of the phase transformation that occurs in the material. The stress-induced phase transformation in Nitinol complicates maintaining a consistent $R$-ratio while following a specific loading scenario,. Therefore, fatigue testing is typically done in strain/displacement control. Additionally, because many Nitinol fatigue specimens are made into geometries such as diamonds or apices, the measured load cannot be directly translated to stress, making it difficult to provide stress-based extrapolations from these tests. Therefore, using a simplified specimen geometry and loading condition, such as a wire in tension, enables simultaneous determination of strain and stress-based properties, and can be used to better understand effects of various loading conditions, including mean stress and $R$-ratio, from a strain/displacement-controlled test.

### 5.2. Crack initiation location

As mentioned previously in Section 4.5, 86 specimens fractured in the gauge section. Out of these 86 fractured specimens, 77 specimens fractured at the FIB-milled starter crack. Looking at the stress amplitude $S$-$N$ curve (Fig. 9), there is a gap between 110 and 100 MPa stress amplitude conditions. The 77 fatigue fractures that originated from the FIB-milled cracks were tested at a stress amplitude of 100 MPa or lower. The nine specimens that fractured in the gauge section but not at the FIB-milled starter crack were tested at stress amplitudes higher than 100 MPa and are represented by the cluster of data points from 135 to 110 MPa stress amplitude in Fig. 9. This observation can be explained by the transition from Type I loading to Type II loading. The difference between these two loading scenarios and their effect on crack initiation and fatigue life of Nitinol is briefly discussed in the following section.

#### 5.2.1. Type I/II loading in superelastic Nitinol

When Nitinol undergoes cyclic deformation off the lower stress plateau, Type I loading refers to the loading in which the far-field stress does not reach the upper plateau stress (UPS). In other words, the cyclic stress range ($\Delta\sigma$) is lower than the difference between the UPS and the lower plateau stress (LPS): $\Delta\sigma < $ UPS-LPS. In this case, the deformation is nominally elastic, $i.e.$, macroscopic stress-induced martensite transformation (SIMT) is not favored, and therefore, the austenite/martensite phase boundaries are not mobile. In Type II loading, however, the far-field stress reaches the upper stress plateau ($\Delta\sigma > $ UPS-LPS). The material undergoes the forward and reverse martensitic phase transformation during each cycle, moving the transformation boundaries

back and forth [47].

In Type I loading, fracture is postulated to initiate at near-surface NMIs in the stable martensite phase, while in Type II loading, fracture is predicted to initiate at zones undergoing cyclic SIMT [47,51]. Accordingly, we hypothesize that the specimens that fractured in the gauge section but not at the FIB starter crack, might have undergone Type II loading compared to specimens that fractured at the FIB-milled starter crack, which would have undergone Type I loading. In Type II loading, cyclic SIMT could be occurring in locations away from the FIB-milled starter crack (e.g. at the transformation front of a Lüder's band), explaining fracture in such locations.

Because stresses in the Type II loading range cyclically induce the forward and reverse martensitic phase transformation, and since these tests are performed at accelerated conditions in non-circulating air, the possibility of localized heating at the transformation front cannot be excluded. Nitinol exhibits a Clausius-Clapeyron relationship between temperature and stress such that the plateau stress values may rise by nominally 4–10 MPa/°C [52]. A rise in temperature may induce a stress elevation therefore shifting the preferred nucleation site to the SIMT front.

Type I loading in air or in a water medium was found to be frequency independent and not effected by adiabatic heating [47]. To verify this in our study, we checked the frequency response of a 20 μm wide FIB starter crack specimen in Type I loading after pre-straining to 6 % and unloading to 3 % mean strain. The specimen was cycled in a continuous waveform at 90 μm displacement amplitude (0.75 % strain amplitude) at 1 Hz, 10 Hz, and 20 Hz for 500 cycles at each frequency condition. The resulting force–displacement plot for this test can be observed in Fig. 14, accordingly no apparent frequency effect is observed.

The transition from Type II to Type I loading can be determined by calculating the normalized stress amplitude, or SA, from the following equation:

$$SA = \frac{\sigma_{max} - \sigma_{min}}{UPS - LPS} \tag{7}$$

when SA > 1 loading is Type II, and when SA < 1 loading is Type I. Using our plateau stress data (UPS = 490 and LPS = 290 MPa), and applying Equation (7) to our stress-based $S$-$N$ data in Fig. 9, we can produce a normalized stress amplitude $S$-$N$ curve highlighting the transition between Type II/I loading for our fatigue data. The normalized stress amplitude $S$-$N$ curve for this study can be observed in Fig. 15, and accordingly the majority of the fatigue data lie below a normalized stress amplitude of 1 (shown by a horizontal dashed line), $i.e.$, it undergoes
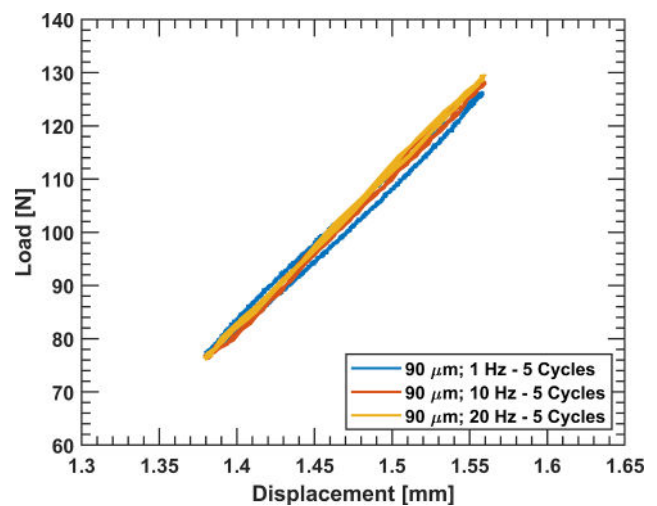


**Fig. 14.** Cyclic force–displacement curve for a 20 μm wide FIB starter crack specimen cycled at 90 μm displacement amplitude (0.75 % strain amplitude) for 5 cycles at 1, 10, and 20 Hz.
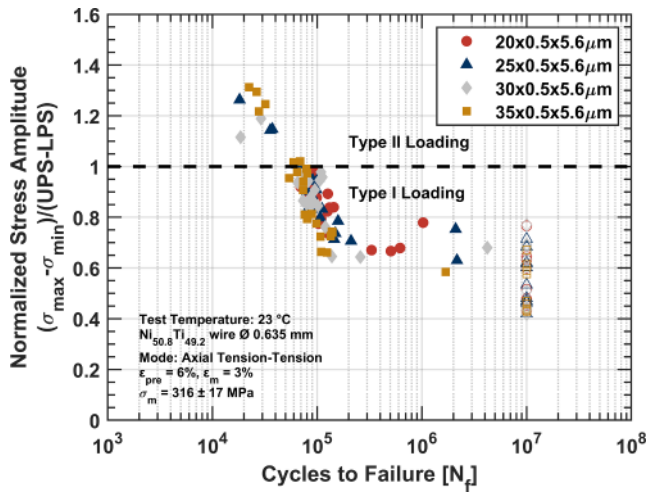
**Fig. 15.** Normalized stress amplitude *vs.* cycles to failure (*S-N*) plot for all the axial tension–tension FIB-milled starter crack Nitinol wire specimens subjected to fatigue testing at 6% pre-strain and 3% mean strain conditions. The horizontal line at 1.0 represents the boundary between Type II/I fatigue loading.

Type I fatigue cycling off the lower plateau. The cluster of data points above this transition line indicates data points obtained from specimens undergoing Type II loading, resulting in fracture away from the FIB-milled starter crack. Type I *vs* Type II loading, and in particular, the significance of applied stress amplitude compared to the *stress hysteresis*, was recently discussed by Launey et al. [17]. They proposed an empirical model for the prediction of the fatigue limit of Nitinol under uniaxial tensile loading based on quasi-static uniaxial tensile data and using the stress hysteresis and cyclic modulus at a given mean strain. Their results, which are consistent with the work by Catoor et al. [47], provide further evidence that the maximum local stresses play an important role on fatigue behavior of superelastic Nitinol, even under displacement/strain-controlled testing condition.

An important fact to keep in mind is the applicability of the loading conditions on the device and principal material parameters that have been determined from the same boundary conditions. Type I loading is common for Nitinol medical devices crimped inside a catheter and deployed at the site of injury where these devices are expected to last 400 to 600 million cycles over their service life.

### 5.3. Small crack growth threshold

Failure of permanent implantable Nitinol medical devices, especially those categorized as Class III, can cause serious harm to the patient. Therefore, it encourages engineers to design such devices to resist crack initiation, as it will be followed by propagation and fracture, likely within a limited number of cycles. The present study enables engineers to incorporate a more conservative fracture mechanics-based material property, *i.e.*, $\Delta K_{th,sc}$, in the design of Nitinol medical devices.

As mentioned earlier, NMIs often act as initiation sites for fatigue cracks in superelastic Nitinol. Moreover, we showed that cyclic SIMT plays an important role in the fatigue behavior of superelastic Nitinol. As discussed by Launey et al., the fatigue limit of Nitinol could therefore be governed by either inclusions (and other types of discontinuities) or SIMT, depending on the inclusion size [17]. In other words, if the inclusions are small, the fatigue limit of Nitinol is dictated by SIMT, however, if they grow larger beyond certain dimensions, the crack initiation threshold from those inclusions could become lower than the SIMT fatigue limit. In that case, $\Delta K_{th,sc}$ required for crack initiation from inclusions or other discontinuities would dictate the fatigue limit of Nitinol.

The $\Delta K_{th,sc}$ threshold is commonly coupled with an operating cyclic

stress range ($\Delta\sigma$) to determine the largest allowable flaw size where no fatigue fracture is expected. The coupling of fatigue crack thresholds with the fatigue limit of a material can be used to create a Kitagawa-Takahashi (KT) diagram to illustrate conditions that are predicted to be safe and not safe from fatigue fracture, incorporating both total life and fracture mechanics-based concepts.

Fig. 16 is the assembled KT diagram for the Nitinol wire material investigated in this study. Robertson and Ritchie were the first to assemble a KT diagram for Nitinol material using superelastic tubing for the manufacture of endovascular stents [22]. Our KT diagram provides an updated and more conservative tool for engineers designing Nitinol medical devices against fatigue fracture compared to the original diagram proposed by Robertson and Ritchie.

Regions where fatigue fracture and no fracture are likely to occur are highlighted in gold and green, respectively. The solid black line delineates the transition between fatigue fracture and no fatigue fracture. The horizontal solid black line is determined from the stress range $\Delta\sigma = 2\,\sigma_{f,a}$, where $\sigma_{f,a}$ is the stress-based fatigue amplitude limit, $\sigma_{f,a} = 45$ MPa. $\Delta K_{th,sc} = 0.34$ MPa$\sqrt{m}$ marks the inflection point and the start of the negative slope of the solid black line where $\Delta\sigma$ decreases with increasing flaw size, represented in terms of the square root of the crack area - $\sqrt{area}$. The gray region between the dashed and solid black lines denotes the differences in the statistically calculated $\sigma_{f,a}$ and $\Delta K_{th,\,sc}$ compared to the highest stress amplitude and $\Delta K_i$ values, below which all specimens survived (stress amplitude = 58 MPa and $\Delta K_i = 0.48$ MPa$\sqrt{m}$).

Previously, the $\Delta K_{th,sc}$ threshold for Nitinol has been reported to range from 1.33 to 0.71 MPa$\sqrt{m}$ for *R*-ratios between 0.1 and 0.7, obtained from crack growth experiments performed on compact-tension specimens harvested from superelastic Nitinol tubes [22]. The $\Delta K_{th,sc}$ (and therefore KT diagram) presented herein is more conservative than those previously reported. This is mainly because, unlike the reported values that were extrapolated from long crack growth data, $\Delta K_{th,sc}$ in the present study was determined from cracks that were fabricated to be on the same size scale or slightly larger than the inclusions contained within the material. Other studies, apart from Robertson and Ritchie, have analyzed Nitinol small crack data from fatigue experiments performed in rotary bend fatigue where the *R*-ratio = -1 [16,18]. These studies observed larger stress intensity values compared to ours for crack
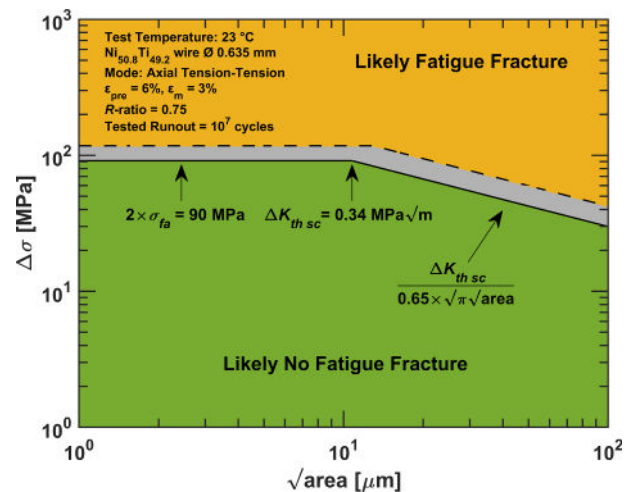


**Fig. 16.** Kitagawa-Takahasi diagram for the 0.635 mm superelastic Nitinol wire used in our study showing regions of safe operation or likely no fatigue fracture (green) along with regions that are at risk for failure from fatigue fracture (gold). The gray region of the plot denotes the difference between our statiscally calculated $\sigma_f$ and $\Delta K_{th,\,sc}$ values compared to those values from experimental testing where runout was observed at or below these values. (For interpretation of the references to colour in this figure legend, the reader is referred to the web version of this article.)

thresholds. The location of fatigue cycling on the stress–strain curve as well as the resulting *R*-ratio cannot be overlooked, as the presence and cycling type of different phases can influence fatigue limit properties. From our study, tension–tension Type I fatigue cycling off the lower plateau stress may produce lower stress-based fatigue limits and $\Delta K_{th,sc}$ values compared to other loading conditions, including for *R*-ratio = -1. It should be noted that increasing the *R*-ratio can decrease the $\Delta K_{th}$ of a material under long crack conditions [29]. In fatigue testing of Nitinol, the plateau stress values and strain/displacement control conditions dictate mean stress and *R*-ratios. Therefore, high *R*-ratios will be inevitable when testing Nitinol in Type I loading.

Fatigue crack propagation thresholds are normally derived from load shedding tests on compact-tension specimens that are undergoing tension–tension loading where no global compressive loading is experienced by the specimen. For *R*-ratio = -1, large compressive loads equal to (or greater than)[3] the tensile loads are subjected to the specimen. This is important to note for Nitinol, as different martensite variants are activated in compressive loading compared to tensile loading and would therefore influence fatigue properties [13,53,54]. Also, the crack closure effect would be more prominent under *R* = -1 conditions, decreasing the $\Delta K$ the specimen experiences and therefore increasing fatigue properties.

One final point is that it is well known that fatigue crack growth threshold stress intensities are significantly lower for small cracks compared to those conventionally measured for long cracks [27], yet in most practical structures, not just medical devices, the total life is dominated by crack propagation when the cracks are small. This has presented a dilemma for lifetimes predictions based on fracture mechanics due to the difficulty of obtaining reliable small crack data. The approach presented in this work provides a methodology for a solution to this issue which was focused on Nitinol devices, but we believe that this approach could be readily adapted for other materials and different structures.

## 6. Conclusions

Our study is the first of its kind to attempt to determine the small crack growth threshold, $\Delta K_{th,sc}$, in superelastic Nitinol using actual small cracks produced from FIB milling while using an experimental hybrid *S-N* and fracture mechanics-based testing approach. In carrying out our testing, we applied pre-strains, mean strains, and cyclic loading conditions (Type I nominally elastic cycling off the lower plateau) relevant to Nitinol medical device applications. Additionally, our experimental testing was conducted under axial tension–tension loading, which is the most appropriate for extrapolating proper fracture mechanics-based material properties. The results of our fatigue testing and analysis have provided the following conclusions:

- The proposed hybrid *S-N* and fracture mechanics-based fatigue testing methodology was able to produce fatigue and fracture mechanics material properties not commonly provided for medical grade superelastic Nitinol. These include a stress-based fatigue limit and small crack growth threshold.
  o The stress-based axial tension–tension fatigue amplitude limit of superelastic Nitinol under Type I loading at $10^7$ cycles was observed to be 45 MPa. This fatigue limit was derived under a pre-strain of 6 %, a mean strain of 3 %, and a mean stress of 316 ± 17 MPa. The fatigue limit was calculated as the 5 % probability of fatigue fracture (*i.e.*, 95 % survival) at 95 % confidence.
  o The small crack growth threshold, or $\Delta K_{th,sc}$, of superelastic Nitinol under Mode I fracture mechanics conditions and Type I loading at $10^7$ cycles was observed to be 0.34 MPa$\sqrt{m}$. This $\Delta K_{th,sc}$ value was derived under a pre-strain of 6 %, a mean strain of 3 %, and an *R* = 0.75. The $\Delta K_{th,sc}$ was calculated as the 5 % probability of fatigue fracture (*i.e.*, 95 % survival) at 95 % confidence.
- Axial tension–tension fatigue fracture occurred at the FIB-milled starter crack only under Type I (fatigue cycling from the lower plateau stress) conditions. Under Type II (fatigue cycling between the upper and lower plateau stresses) loading conditions, fatigue fracture was observed in a limited number of instances to occur in the gauge length of the specimens but away from the FIB-milled starter crack.
- From the data set, we were able to assemble a refined and more conservative Kitagawa-Takahashi diagram for use by medical device designers and engineers.

## CRediT authorship contribution statement

**Louis G. Malito:** Writing – original draft, Supervision, Resources, Project administration, Methodology, Investigation, Formal analysis, Data curation, Conceptualization. **Behrouz Haghgouyan:** Writing – original draft, Formal analysis, Conceptualization. **Matthew L. Bowers:** Writing – original draft, Supervision. **Alfred Rosen:** Data curation. **Behnam Amin-Ahmadi:** Data curation. **Scott W. Robertson:** Writing – original draft, Supervision, Conceptualization. **Robert O. Ritchie:** Writing – original draft, Supervision, Conceptualization.

## Declaration of competing interest

The authors declare that they have no known competing financial interests or personal relationships that could have appeared to influence the work reported in this paper.

## Data availability

Data will be made available on request.

## Acknowledgements

---

[3] Due to the tension–compression asymmetry, nominally the plateau stress is cited to be a 1.5X larger in compression.

## References

[1] Duerig T, Pelton A, Stöckel D. An overview of nitinol medical applications. Mater Sci Eng A 1999;273:149–60.
[2] Pelton AR. Evaluation of mechanical fatigue and durability. Handbook of Vascular Motion Elsevier 2019:313–35.
[3] Pelton AR, Schroeder V, Mitchell MR, Gong XY, Barney M, Robertson SW. Fatigue and durability of Nitinol stents. J Mech Behav Biomed Mater 2008;1:153–64. https://doi.org/10.1016/j.jmbbm.2007.08.001.
[4] Robertson SW, Launey M, Shelley O, Ong I, Vien L, Senthilnathan K, et al. A statistical approach to understand the role of inclusions on the fatigue resistance of superelastic Nitinol wire and tubing. J Mech Behav Biomed Mater 2015;51: 119–31.
[5] Pelton AR. Nitinol fatigue: a review of microstructures and mechanisms. J Mater Eng Perform 2011;20:613–7.
[6] Cao H, Wu MH, Zhou F, McMeeking RM, Ritchie RO. The influence of mean strain on the high-cycle fatigue of Nitinol with application to medical devices. J Mech Phys Solids 2020:104057.

[7] Launey M, Robertson SW, Vien L, Senthilnathan K, Chintapalli P, Pelton AR. Influence of microstructural purity on the bending fatigue behavior of VAR-melted superelastic Nitinol. J Mech Behav Biomed Mater 2014;34:181–6.

[8] Senthilnathan K, Shamimi A, Bonsignore C, Paranjape H, Duerig T. Effect of prestrain on the fatigue life of superelastic nitinol. J Mater Eng Perform 2019;28: 5946–58.

[9] Runciman A, Xu D, Pelton AR, Ritchie RO. An equivalent strain/Coffin–Manson approach to multiaxial fatigue and life prediction in superelastic Nitinol medical devices. Biomaterials 2011;32:4987–93.

[10] Adler P, Frei R, Kimiecik M, Briant P, James B, Liu C. Effects of tube processing on the fatigue life of nitinol. Shape Memory and Superelasticity 2018;4:197–217.

[11] Schaffer JE, Plumley DL. Fatigue performance of nitinol round wire with varying cold work reductions. J Mater Eng Perform 2009;18:563–8. https://doi.org/10.1007/s11665-009-9363-4.

[12] Pelton AR, Fino-Decker J, Vien L, Bonsignore C, Saffari P, Launey M, et al. Rotary-bending fatigue characteristics of medical-grade Nitinol wire. J Mech Behav Biomed Mater 2013;27:19–32.

[13] Malito LG, Briant PL, Bowers ML, Easley S, Schaffer JE, James B. Fatigue, fracture, and crack arrest from bending induced pre-strain in superelastic Nitinol. Shape Memory and Superelasticity 2022:1–13.

[14] Robertson SW, Pelton AR, Ritchie RO. Mechanical fatigue and fracture of Nitinol. Int Mater Rev 2012;57:1–37. https://doi.org/10.1179/1743280411Y.0000000009.

[15] Schaffer JE. Mechanical conditioning of superelastic nitinol wire for improved fatigue resistance. J ASTM Int 2010;7:1–7.

[16] Urbano MF, Cadelli A, Sczerzenie F, Luccarelli P, Beretta S, Coda A. Inclusions size-based fatigue life prediction model of NiTi alloy for biomedical applications. Shape Memory and Superelasticity 2015;1:240–51.

[17] Launey ME, Ong I, Berg BT, Pelton AR. Considerations on tension-tension fatigue predictions for Nitinol. Shape Memory and Superelasticity 2023;9:97–115.

[18] Weaver JD, Sena GM, Aycock KI, Roiko A, Falk WM, Sivan S, et al. Rotary bend fatigue of nitinol to one billion cycles. Shape Memory and Superelasticity 2023: 1–24.

[19] Pelton AR, Berg BT, Saffari P, Stebner AP, Bucsek AN. Pre-strain and mean strain effects on the fatigue behavior of superelastic nitinol medical devices. Shape Memory and Superelasticity 2022;8:64–84. https://doi.org/10.1007/s40830-022-00377-y.

[20] Mahtabi MJ, Shamsaei N, Mitchell MR. Fatigue of Nitinol: the state-of-the-art and ongoing challenges. J Mech Behav Biomed Mater 2015;50:228–54. https://doi.org/10.1016/j.jmbbm.2015.06.010.

[21] Robertson SW, Ritchie RO. In vitro fatigue–crack growth and fracture toughness behavior of thin-walled superelastic Nitinol tube for endovascular stents: a basis for defining the effect of crack-like defects. Biomaterials 2007;28:700–9.

[22] Robertson SW, Ritchie RO. A fracture-mechanics-based approach to fracture control in biomedical devices manufactured from superelastic Nitinol tube. J Biomed Mater Res B Appl Biomater 2008;84:26–33.

[23] McKelvey AL, Ritchie RO. Fatigue-crack propagation in Nitinol, a shape-memory and superelastic endovascular stent material. Journal of Biomedical Materials Research: An Official Journal of The Society for Biomaterials, The Japanese Society for Biomaterials, and The Australian Society for Biomaterials and the Korean Society for Biomaterials 1999;47:301–8.

[24] McKelvey AL, Ritchie RO. Fatigue-crack growth behavior in the superelastic and shape-memory alloy Nitinol. Metall Mater Trans A 2001;32:731–43.

[25] Pelton AR, Russell SM, DiCello J. The physical metallurgy of nitinol for medical applications. JOM 2003. https://doi.org/10.1007/s11837-003-0243-3.

[26] Rahim M, Frenzel J, Frotscher M, Pfetzing-Micklich J, Steegmüller R, Wohlschlögel M, et al. Impurity levels and fatigue lives of pseudoelastic NiTi shape memory alloys. Acta Mater 2013;61:3667–86.

[27] Suresh S, Ritchie RO. Propagation of short fatigue cracks. International Metals Reviews 1984;29:445–75.

[28] Ritchie RO, Lankford J. Small fatigue cracks: a statement of the problem and potential solutions. Mater Sci Eng 1986;84:11–6. https://doi.org/10.1016/0025-5416(86)90217-X.

[29] Suresh S. Fatigue of materials. Cambridge University Press; 1998.

[30] Paris P, Erdogan F. A critical analysis of crack propagation laws. J. Basic Eng. 1963.

[31] McCarver JF, Ritchie RO. Fatigue crack propagation thresholds for long and short cracks in René 95 Nickel-base superalloy. Mater Sci Eng 1982;55:63–7.

[32] Roiko A, Solin J. Measurement of small cracks initiating from inclusions, Focused Ion Beam notches and drilled holes. Int J Fatigue 2014;62:154–8.

[33] Murakami Y, Matsunaga H, Abyazi A, Fukushima Y. Defect size dependence on threshold stress intensity for high-strength steel with internal hydrogen. Fatigue Fract Eng Mater Struct 2013;36:836–50.

[34] Li B, Koyama M, Sakurada E, Yoshimura N, Ushioda K, Noguchi H. Potential resistance to transgranular fatigue crack growth of Fe–C alloy with a supersaturated carbon clarified through FIB micro-notching technique. Int J Fatigue 2016;87:1–5.

[35] Murakami Y, Endo M. Quantitative evaluation of fatigue strength of metals containing various small defects or cracks. Eng Fract Mech 1983;17:1–15.

[36] Murakami Y, Endo M. Effects of defects, inclusions and inhomogeneities on fatigue strength. Int J Fatigue 1994;16:163–82.

[37] Murakami Y. Metal fatigue: effects of small defects and nonmetallic inclusions. Academic Press; 2019.

[38] Couroneau N, Royer J. Simplified model for the fatigue growth analysis of surface cracks in round bars under mode I. Int J Fatigue 1998;20:711–8.

[39] Shin CS, Cai CQ. Experimental and finite element analyses on stress intensity factors of an elliptical surface crack in a circular shaft under tension and bending. Int J Fract 2004;129:239–64.

[40] Newman Jr JC, Raju IS. An empirical stress-intensity factor equation for the surface crack. Eng Fract Mech 1981;15:185–92.

[41] Daly S, Miller A, Ravichandran G, Bhattacharya K. An experimental investigation of crack initiation in thin sheets of nitinol. Acta Mater 2007;55:6322–30.

[42] Haghgouyan B, Hayrettin C, Baxevanis T, Karaman I, Lagoudas DC. Fracture toughness of NiTi–Towards establishing standard test methods for phase transforming materials. Acta Mater 2019;162:226–38.

[43] Robertson SW, Mehta A, Pelton AR, Ritchie RO. Evolution of crack-tip transformation zones in superelastic Nitinol subjected to in situ fatigue: a fracture mechanics and synchrotron X-ray microdiffraction analysis. Acta Mater 2007;55: 6198–207.

[44] Gollerthan S, Young ML, Neuking K, Ramamurty U, Eggeler G. Direct physical evidence for the back-transformation of stress-induced martensite in the vicinity of cracks in pseudoelastic NiTi shape memory alloys. Acta Mater 2009;57:5892–7. https://doi.org/10.1016/j.actamat.2009.08.015.

[45] Haghgouyan B, Young B, Picak S, Baxevanis T, Karaman I, Lagoudas DC. A unified description of mechanical and actuation fatigue crack growth in shape memory alloys. Acta Mater 2021;217:117155.

[46] ATSM F2004, Standard Test Method for Transformation Temperature of Nickel-Titanium Alloys by Thermal Analysis, 13.01 (2017) 1–5. 10.1520/F2004-17.

[47] Catoor D, Ma Z, Kumar S. Cyclic response and fatigue failure of Nitinol under tension–tension loading. J Mater Res 2019;34:3504–22.

[48] ASTM E1823, Standard Terminology Relating to Fatigue and Fracture Testing, Annual Book of ASTM Standards 03.01 (2020) 1–25. 10.1520/E1823-20B.2.

[49] Lopes TL, Gong X-Y, Trépanier C. Fatigue performance of nitinol tubing with Af OF 25 C. in: SMST 2003: Proceedings of the International Conference on Shape Memory and Superelastic Technologies 2004:311.

[50] Alarcon E, Heller L, Chirani SA, Šittner P, Kopeček J, Saint-Sulpice L, et al. Fatigue performance of superelastic NiTi near stress-induced martensitic transformation. Int J Fatigue 2017;95:76–89.

[51] Zheng L, He Y, Moumni Z. Lüders-like band front motion and fatigue life of pseudoelastic polycrystalline NiTi shape memory alloy. Scr Mater 2016;123:46–50.

[52] Duerig TW, Bhattacharya K. The influence of the R-phase on the superelastic behavior of NiTi. Shape Memory and Superelasticity 2015;1:153–61.

[53] Duerig TW. Some unsolved aspects of Nitinol. Mater Sci Eng A 2006;438–440: 69–74. https://doi.org/10.1016/j.msea.2006.05.072.

[54] Gupta S, Pelton AR, Weaver JD, Gong XY, Nagaraja S. High compressive pre-strains reduce the bending fatigue life of nitinol wire. J Mech Behav Biomed Mater 2015; 44:96–108. https://doi.org/10.1016/j.jmbbm.2014.12.007.